Assimilation of Airborne Imagery with LIDAR for Bathymetric Estimation

by

Chadwick L. Monfort

A THESIS

Submitted to

The Ohio State University

5/16/08

ABSTRACT

For predictive means it is important to know the underlying bathymetry of the nearshore coastline, however, this region's turbulent nature and tendency to develop rapidly over large scales make it difficult to survey. A better capability to measure bathymetry over large scales is a crucial step in better understanding nearshore processes and protecting infrastructure from erosion. An airborne Light Detecting and Ranging (LIDAR) system has the ability to survey large geographic areas over both dry land and shallow water, while maintaining a high rate of data collection, making it ideal for the study of coastal regions. Bathymetric LIDAR is dependent on water clarity, and in the surf zone sediment and air bubbles entrained in the water column by wave breaking compromise its ability to retrieve accurate bottom elevations. This work explores the potential of data assimilation techniques to estimate bathymetry in regions where airborne LIDAR fails. This is accomplished using pixel intensities extracted from time-averaged airborne imagery and scaled appropriately to be representative of spatial patterns of energy dissipation due to wave breaking. Following Van Dongeren, *et al*. (2008), differences between scaled image pixel intensity patterns and dissipation patterns numerically calculated using a wave model were iteratively converged upon by appropriately modifying an initially estimated bathymetry. Final assimilated bathymetry estimates were compared to surveyed bathymetry data collected at the USACE Field Research Facility in Duck, NC using traditional methods. Analysis of data sets from several dates produced RMS errors between assimilated and surveyed bathymetry to be typically around 35 *cm*.

This is dedicated to my family and friends.

ACKNOWLEDGMENTS

Special thanks to Dr. Tom Lippmann for giving me this opportunity to learn and for all the help which he has given to me along the way. I would also like to thank the people at the USGS Center for Coastal and Watershed Studies as well as the USACE JALBTCX for their generous support.

TABLE OF CONTENTS

LIST OF FIGURES

Figure 16: A plot of scaled image intensity (black, *watts/m*^{2}) and final wave model dissipation (green, *watts/m*^{2}) above left with actual (red, *m*) and final estimated (blue, *m*) crosshore bathymetric profiles shown (below left). The same figure is showed zoomed in to the surf zone region of the profile (right).

Figure 17: A contour plot of the FRF surf zone created from a data set of assimilated bathymetric profiles from 2002/04/13 (top left), a contour plot of the FRF surf zone created from a data set of intially estimated bathymetric profiles from 2002/04/13 (top right), and a contour plot of the FRF surf zone created from a data set of FRF surveyed bathymetric profiles from 2002/04/17 (bottom left). Crosshore coordinate is given for the x-axis and alongshore coordinate for the y-axis in all figures.

Figure 18: A contoured difference plot of the FRF surf zone between initially estimated bathymetry from 2002/04/13 and FRF surveyed bathymetry from 2002/04/17 (left) and a contoured difference plot of the FRF surf zone between assimilated bathymetry from 2002/04/13and FRF surveyed bathymetry from 2002/04/17(right). Crosshore coordinate is given for the x-axis and alongshore coordinate for the y-axis in both figures. A contour color map is given for each figure as well.

Figure 19: Bathymetry RMS error plotted as a function of crosshore coordinate for both initial and assimilated bathymetric estimates (left), and bathymetry RMS error plotted as a function of alongshore coordinate for both initial and assimilated bathymetric estimates (right). Data for both plots was collected between 2002/04/13 and 2002/04/17.

Figure 20: Average bathymetric RMS error plotted as a function of sigma showing optimal results around four degrees.

I. Introduction

Ocean and land meet at the beach in a contradictory show of turbulent force and tranquil beauty that has intrinsically always drawn human interest. This display is generated by the complex physical processes of nearshore coastal evolution that continually shape the coastal environment through erosion and accretion of sand. Although these processes are very important because of their far reaching impacts, we do not yet fully understand them. A desire to better understand nearshore coastal evolution is motivated by the need to protect the many human interests in the beach and surrounding areas.

The beach is much more than a place to build a sand castle, its aesthetic and recreational value drives a multi-billion dollar tourist industry. International tourism to beaches in the United States is estimated to generate 134 million dollars a year (Houston, 1996). The revenue generated from tourism supports the economies of coastal communities, is the major source of income for over 1.4 million businesses, and creates significant job opportunities (Houston, 1996). Coastal erosion, caused by processes of nearshore coastal evolution, degrades the quality of beaches and threatens local tourism. Coastal erosion occurs when nearshore currents, wave actions, and sediment sources cause a net transport of sand away from the beach to offshore locations. Attempts to revitalize beaches through various nourishment projects are extremely expensive and have thus far been proven to offer only temporary results. Regardless of this, many coastal communities find it necessary to do so in order to ensure tourist keep coming to their beaches.

Although they may have to put up with a constant influx of tourists, large cities have historically been located on the coast because of the benefits associated with having easy access to both land and ocean resources. Due to their strategic location, coastal cities are the site of commercial, industrial, and marine infrastructure that are vital for national security and economic

purposes. It is estimated that nearly one-half the world's population lives within 50 miles of the ocean, a fact which makes it hard to understate the importance of the beach (Dalrymple, 2003). The beach serves as a natural barrier that protects people and infrastructure from the destructive potential of the ocean. The phenomenon of nearshore coastal evolution has long been a challenge to permanent human settlement near the beach because erosion puts valuable beach properties at risk to the forces of waves and currents. Nearshore bathymetry and beach topography are also critical in limiting shoreline erosion during storms. Man made barriers, such as sea walls, are often erected as a preventative measure, but these structures can actually increase erosion rates, perpetually worsening the situation (Kraus and McDougal, 1996). An ever increasing human impact combined with rising sea levels will only serve to amplify the problem of shoreline erosion in the future.

To address this issue effectively we must better understand the factors that influence nearshore coastal evolution. The primary mechanism of coastal sediment transport and erosion is the energy dissipated by waves as they progress shoreward through the surf zone. These forces are difficult to directly measure, but can indirectly be inferred if we know the underlying bathymetry. In the shallow nearshore region (within a few hundred meters of the shoreline), the bathymetry largely dictates wave evolution and is thus of the upmost importance. The complex nature of the nearshore, along with its tendency to develop rapidly over large scales, makes it a very difficult region to measure bathymetry. Traditional methods utilize Global Positioning Systems (GPS) and sonar altimeters onboard mobile platforms to accurately measure bathymetry, but can only be applied to relatively small areas because these techniques involve intense manual labor. Typical nearshore processes occur on scales on the order of 10's to 100's of kilometers, making traditional methods useful to only specific local regions. The ability to

collect accurate bathymetry over these large scales is thus an essential requirement for quantifying sediment transport, determining areas of coastlines at risk to erosion and storm damage, and for general research of large scale coastal behavior (LSCB).

Advancements in GPS and Inertial Navigation Systems (INS) technology have led to the development of airborne LIDAR (Figure 1). An airborne LIDAR system works by transmitting laser pulses from an aircraft at an extremely high frequency (20,000 *Hz*). Using the travel time from emission to return of each laser pulse, together with accurate orientation information provided by an integrated GPS/INS system, LIDAR can define ground elevations within +/- 2 *m* horizontally +/-15 *cm* vertically (Irish *et al*, 2000). Using a green wavelength laser to penetrate the water column, LIDAR is also able to collect submarine topographic data with limitations depending on water clarity and depth (Figure 1). Airborne LIDAR has the capability to accurately sample large geographic areas in relatively short periods of time, making it ideal for large scale studies of coastal regions. It is currently being used for coastal mapping and storm impact studies throughout North America, where water clarity allows for bottom detection.

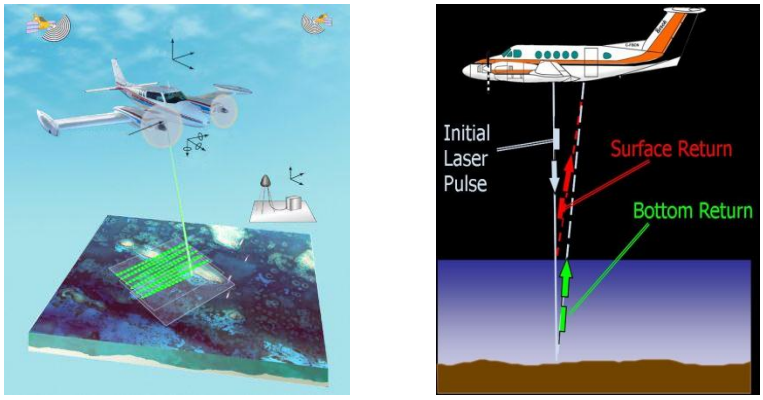

Figure 1: A diagram of an airborne LIDAR system and components (left) and a diagram of red and green wavelength laser returns as transmitted from an airborne LIDAR system (right).

In the surf zone, air bubbles and sediment entrained in the water column impede the ability of LIDAR to accurately obtain sea bottom elevation data. The surf zone plays an important role in wave energy dissipation and limits the usefulness of airborne LIDAR. Current LIDAR systems must either wait for deployment during calm wave conditions to avoid this issue or are restricted to collecting topographic data only. It would be advantageous for both industry and science that examine LSCB to improve on the capabilities of estimating bathymetry data in the surf zone.

Data assimilation methods have been established for estimating bathymetry in the surf zone using known offshore wave conditions and time-averaged imagery obtained from land-based video systems (Figure 2; Aarninkhof and Ruessink, 2004; Aarninkhof, *et al*., 2004; Roelvink, *et al.*, 2006). Data assimilation techniques are based on the principles of conservation of wave energy and momentum. As a wave breaks in the surf zone, the wave dissipates its energy as heat and turbulence. On typical sandy beaches, dissipation by bottom friction is considered negligible and energy loss due to wave breaking is the primary dissipative mechanism (Thornton and Guza, 1986).

Figure 2: A time-averaged image of the coastline taken from an obliquely oriented land-based camera.

The crosshore wave energy flux balance can be used to model wave transformation across the surf zone.

$$\frac{\partial}{\partial x}\left(E_w c_g \cos\alpha\right) = \varepsilon_r \quad (1)$$

Where ε_r is dissipation due to wave breaking, c_g is the group velocity, α is the wave angle, and $E_w = 1/8\,\rho g H^2$ is the linear wave theory energy with variables ρ for density, g for gravity, H for wave height, and x for crosshore location.

Dissipation due to wave breaking, $\varepsilon_r = \tau_s c$, can be written as a function of the shear stress at wave interface, τ_s, and the wave phase speed c (Deigaard, 1993). Following LeMahaute (1962) the dissipation can also be written in terms of wave frequency, f, local water depth, h, and the adjustable parameter B of order one.

$$\varepsilon_r = -\frac{1}{4} B^3 \rho g f \frac{H^3}{h} \quad (2)$$

The simple wave model used in this work includes the concept of a wave roller, an elevated body of turbulent water created by wave breaking and riding on the front face of the wave (Svendson, 1984). The wave roller energy flux is incorporated into the wave model to more accurately describe the crosshore distribution of dissipation (Lippmann, *et al*., 1996). In this wave model, the wave roller energy flux gradient is given by $\partial/\partial X\,(E_r c \cos\alpha)$, where E_r is the energy in the wave roller. Incorporating the wave roller term into the overall energy flux balance (1) gives:

$$\frac{\partial}{\partial x}\left(E_w c_g \cos\alpha\right) + \frac{\partial}{\partial x}\left(E_r c \cos\alpha\right) = -\frac{1}{4} B^3 \rho g f \frac{H^3}{h} \quad (3)$$

Equation (3) has been derived under the assumption that the energy transformation at a given location is represented by a single wave. In the real world, the wave field is comprised of a spectrum of random wave heights that break in a distribution that transforms across the surf zone. This is incorporated into the energy flux balance by ensemble averaging the total wave field through the Raleigh distribution, $p(H)$, and a modified Raleigh distribution determined empirically to describe the breaking wave distribution, $p_b(H)$. This equation is given as follows

$$\langle \frac{\partial}{\partial x}\left(E_w c_g \cos\alpha\right)\rangle + \langle \frac{\partial}{\partial x}\left(E_r c \cos\alpha\right)\rangle = \langle -\frac{1}{4} B^3 \rho g f \frac{H^3}{h}\rangle \tag{4}$$

where $\langle \quad \rangle$ indicates ensemble averaging (Thornton and Guza, 1983). Carrying out the integration on (4) following Lippmann *et al.* (1996) yields

$$\frac{\partial}{\partial x}\left(\frac{1}{8} {H_{rms}}^2 c_g\right) + \frac{3f\sqrt{\pi}}{4\tan\sigma}\frac{\partial}{\partial x}\left[M H_{rms}^3 \cos\alpha\left(1 - \frac{1}{(1+(H_{rms}/\gamma h)^2)^{5/2}}\right)\right] =$$

$$\frac{3\sqrt{\pi}}{2} f M \frac{{H_{rms}}^3}{h}\left(1 - \frac{1}{(1+(H_{rms}/\gamma h)^2)^{5/2}}\right) \tag{5}$$

where H_{rms} is the root-mean-square wave height, γ is an energy saturation coefficient, σ is the wave/roller interface angle, and $M = 1 + \tanh[8(H_{rms}/\gamma h - 1)]$ is a weighting function defined by Whitford (1988).

The wave height distribution is then found using a simple forward stepping algorithm:

$$(E_w c_{cx})_2 + (E_r c_x)_2 = \langle \varepsilon_r \rangle \Delta x + \left(E_w c_{gx}\right)_1 + (E_r c_x)_1 \tag{6}$$

where the H_{rms} value at the next shoreward profile location is found knowing the previous H_{rms} value and calculated dissipation (Thornton and Guza, 1983). This method works only if the water depths are known. In many cases, including the observed case of airborne LIDAR, the

actual bathymetry is often incomplete or not known at all. As a consequence, dissipation patterns in the nearshore cannot be calculated from incomplete LIDAR profiles. Assimilation techniques are able to iteratively calculate bathymetry when it is not available by using information obtained from time-averaged imagery. Previous work using data assimilation techniques have concentrated on creating time-averaged mosaics from video data collected by an obliquely oriented land-based camera. In this work, we will utilize image data collected by an aerial video system (AVS).

In any image of the surf zone, spatial patterns of wave dissipation due to breaking over submerged topography are manifested visually as brightness from foam and turbulence (Lippmann and Holman, 1987). If image data are accurately transformed to an appropriate ground coordinate system, spatial patterns of time-averaged image pixel intensities can be assumed representative of true dissipation patterns. The strong correlation that exists between bathymetry and dissipation (Figure 3; Lippmann, *et al.*, 1993), which can mathematically be related by the wave model described previously, is the basis of assimilation techniques that utilize time-averaged video imagery to estimate nearshore bathymetric profiles (Aarninkhof and Ruessink, 2004; Roelvink, *et al.*, 2006). Assuming that the wave field dissipates all

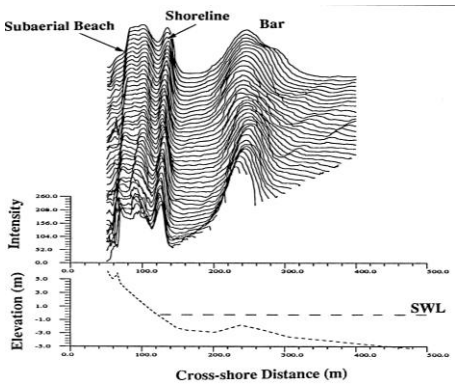

Figure 3: A plot showing the correlation of scaled image intensities (on top) to bathymetric/topographical features (on bottom).

of its energy through the surf zone, image intensity values can be scaled by the offshore energy flux using a constant denoted by λ:

$$E_{w_o} = \lambda \int_0^\infty \langle I \rangle \, dx = \int_0^\infty \langle E_r \rangle \, dx \tag{7}$$

allowing scaled image intensities to be compared to dissipation numerically calculated by a wave model.

If the surf zone bathymetry is not initially known, it must be assumed and input into the wave model along with known wave conditions to numerically predict initial dissipation distributions. A corresponding profile of image intensity is extracted from a time-averaged mosaic from the same crosshore location, normalized by λ, and compared to the dissipation calculated using the wave model. The initially estimated bathymetry can then be updated as a function of difference between scaled intensity and calculated dissipation in a manner that brings the two into closer agreement (Figure 4). This assimilation process is iteratively repeated

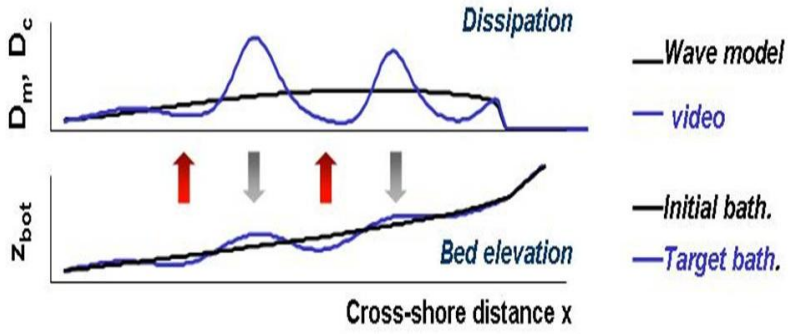

Figure 4: A plot of scaled image intensities and wave model dissipation (above) and corresponding regions where erosion and accretion must be applied to the initial bathymetry to reach the target bathymetry (bottom).

until the difference between the scaled image intensities and modeled dissipation are within a reasonable error tolerance, at which point the assimilated bathymetry becomes the final estimate. Previous work using similar data assimilation techniques with land-based imagery to estimate

bathymetry have produced results with typical RMS values around 30 *cm*.

II. Methods

This work uses topographic and bathymetric data collected by two independently operated airborne LIDAR systems: 1) the Army Corps of Engineers Compact Hydrographic Airborne Rapid Total Survey (CHARTS) system based at Stennis International Airport, MS and operated on a continual basis around the world through JALBTCX (The Joint Airborne LIDAR Bathymetry Technical Center of Expertise), and 2) the NASA operated EAARL (Experimental Advanced Airborne Research LIDAR) system utilized by the USGS Center for Coastal Studies in St. Petersburg, FL for primary use in storm response studies. Processed data sets, filtered for noise by personnel at JALBTCX and the USGS, were acquired from hard disk copies as well as ftp download from the JALBTCX website. Easting, northing, and elevation data were extracted from the original processed data sets, cropped to the area of interest along the North Carolina coastline, and saved as a comma delimited text file. Each of these modified data sets were then imported into ArcGIS where they were first converted into a Triangulated Irregular Network (TIN), which were then used to interpolate data onto an evenly spaced *2* x *2 m* Digital Elevation Model (DEM) raster grid (Figure 5). The raster grid is then imported into Fledermaus where

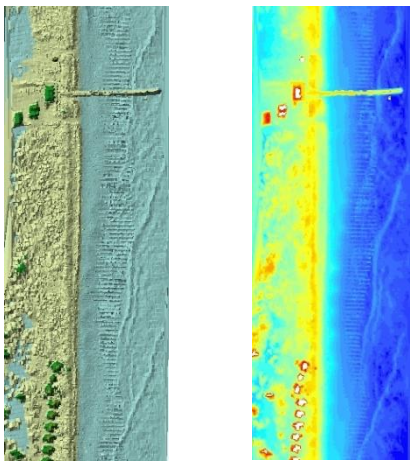

Figure 5: An example of a TIN data set (left) and a DEM raster data set (right).

it is finally exported as a x,y,z text file. These data sets can be used in Matlab to extract bathymetric profiles that extend from the shoreline (defined here as the crosshore coordinate having elevation equal to the approximate tide level at the time of data collection) to a point offshore (in our case 900 *m* offshore).

Operational LIDAR systems collect standard visible band color video imagery concurrently with topographical data. The video is sampled at nominally 1*Hz* and is stored digitally as independent image files. Each image is synchronized to the GPS within a few milliseconds and associated with a roll, pitch, and heading determined from the associated INS. Hard disk copies of raw CHARTS image files along with associated navigation files were available and tested for their potential usefulness in the creation of time-averaged mosaics for the purpose of assimilation.

Necessary orientation parameters were extracted from the navigation files and formatted for use with Erdas Imagine Photogrammetric Software Suite for ortho-rectification of the raw images. This required the conversion of roll, pitch, and heading to the Ω, Φ, K rotation system (Morris, 1966) and creation of an Erdas position file that included information for image number, image name, camera position, as well as Ω, Φ, K values. The Erdas position file along with intrinsic camera parameters for focal length, pixel size, and tertiary radial lens distortion coefficients were imported into Erdas Imagine where a batch operation executed the ortho-rectification of an entire raw image data set to a ground resolution of 2 *m*. Ortho-rectified images were stored in a grayscale (1:255) tiff format.

The CHARTS system flies at a relatively low altitude and high speed that are optimal for collection of LIDAR data, but result in video images with uncertain image orientation and

insufficient image overlap that eliminate their potential usefulness for creation of time-averaged mosaics (Figure 6). Furthermore, to save computer disk space CHARTS imagery is converted to a compressed jpeg format during the collection process which severely reduces its quality (Figure 6). As a result of poor LIDAR image quality, CHARTS imagery, and consequently LIDAR bathymetry data, could not be used for testing of assimilation techniques.

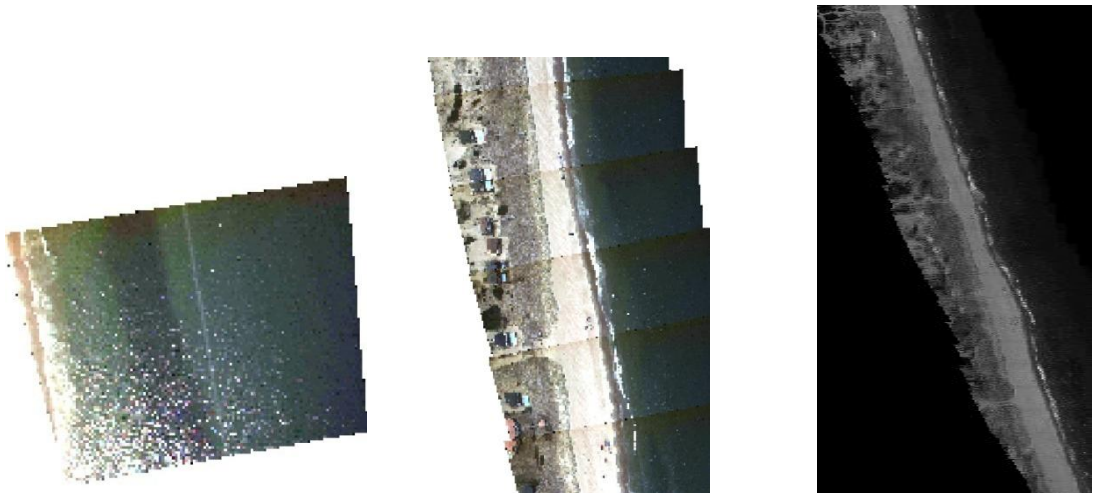

Figure 6: An example of an individual CHARTS .jpg image (left), a section of overlayed CHARTS images showing lack of overlap between individual images (center), and a time-averaged mosaic created from CHARTS imagery (right).

The bathymetry was instead obtained using traditional survey methods by the USACE Field Research Facility (FRF) in Duck, NC. FRF bathymetric data sets are collected on a regular basis and contain individual profile transects spanning the 1500 *m* stretch of coastline surrounding the facilities' research pier (Figure 7), which became the primary area of focus for this study. To test the assimilation methods, the FRF data were used to synthetically create a LIDAR surveyed bathymetry map. The portion of each FRF bathymetric survey in the

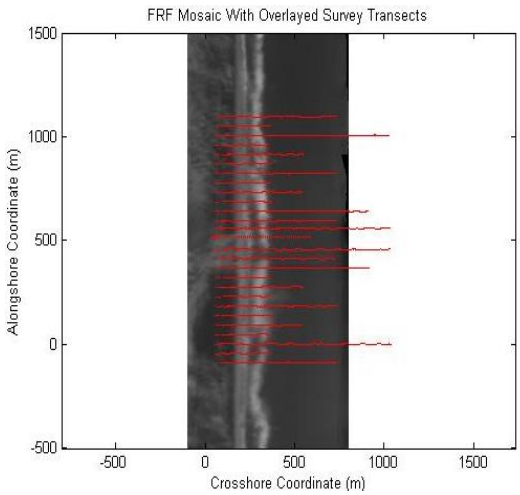

Figure 7: An example of a complete set of FRF surveyed bathymetric profiles (red) overlaid on a time-averaged mosaic of the pier and surrounding area.

surf zone was thrown out. The data are assumed representative of an incomplete LIDAR data set (Figure 8) in which the depth retrievals in the surf zone were compromised.

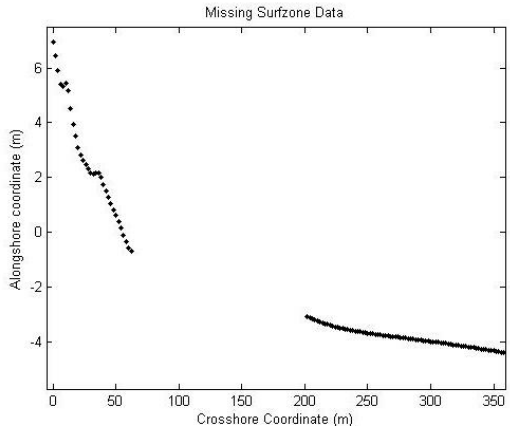

Figure 8: A plot of a FRF surveyed crosshore bathymetry profile with data from the surf zone removed.

To test the assimilation methods, this work uses uncompressed image data collected by an independent AVS system (Figure 9; Worley, *et al*., 1997; Worley, *et al*., 1998) that is operated at a higher altitude and lower speed than that of typical LIDAR systems. The AVS is operated in a way that could be achieved by current LIDAR systems with adjustments to their standard

operating procedures. To better deal with the extremely large data sets provided by this AVS, they are broken into individual north/south run data sets spanning from Cape Hatteras to the

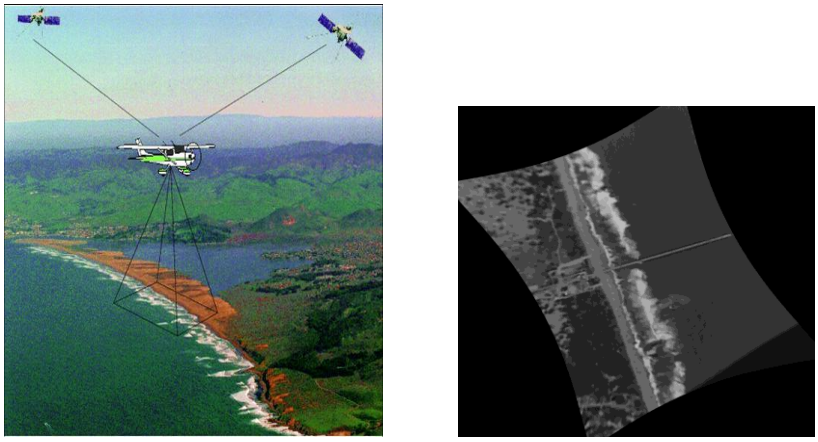

Figure 9: A diagram of an airborne video system and components (left) and an individual tiff image taken by the AVS system used for analysis in this work (right).

North Carolina-Virginia border. The image data utilized for assimilation in this work had synchronized GPS data, but did not provide any image orientation information.

The same procedures described above for image ortho-rectification of the CHARTS imagery were used again, except the pitch and roll were assumed to be zero, and a process to obtain heading information from the GPS was added. This process entailed creating a sample data set of rectified images at an interval so that only the edges of each image overlapped (an interval of every 80 images was commonly used). This sample data set was plotted in ArcGIS where individual images were checked for heading biases by observing the alignment of permanent fixtures such, as the sand dunes from image to image, as well as the alignment of ground check points where available. This process was done iteratively until the sample image data set appeared to be properly aligned, at which point the estimated biases were linearly interpolated through the entire data set and applied to fix heading values. Biases associated with

small pitch and roll can largely be ignored because their effects become minimal after averaging. In cases with large pitch and roll bias the data were thrown out.

Once the images have been successfully ortho-rectified with heading bias corrections, they are ready for mosaicing. An initial attempt was made to use Erdas Imagine for image mosaicing, but because it did not have the proper averaging functions, it was instead necessary to develop a Matlab program for this purpose. This program separates each north/south data set into 21 sections each defined by a USGS baseline along the North Carolina coastline. Pixel intensities from each individual image within a given section are assigned a cell position within a geo-referenced matrix based on their real world UTM coordinates at a 2 *m* resolution (Figure 10). The matrix is averaged by dividing the sum of pixel intensity values in a given cell

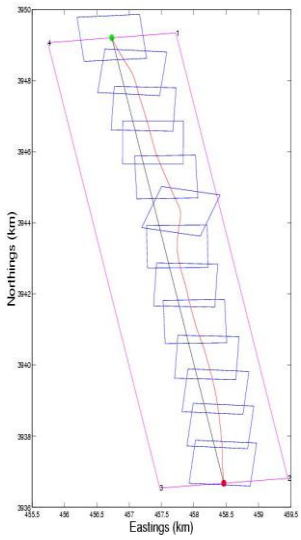

Figure 10: A visual depiction of the time-average mosaic process.

position by the total number of pixels that were added to that cell and then saved as a geo-referenced tiff image file. This is done for each section covered by the flight path after which each mosaic section is rotated into the baseline coordinate system. Finally, mosaic sections are

further averaged 20 *m* in the alongshore direction to improve the relationship between image intensity and bathymetric features (Figure 11). At this point, AVS time-averaged image mosaics

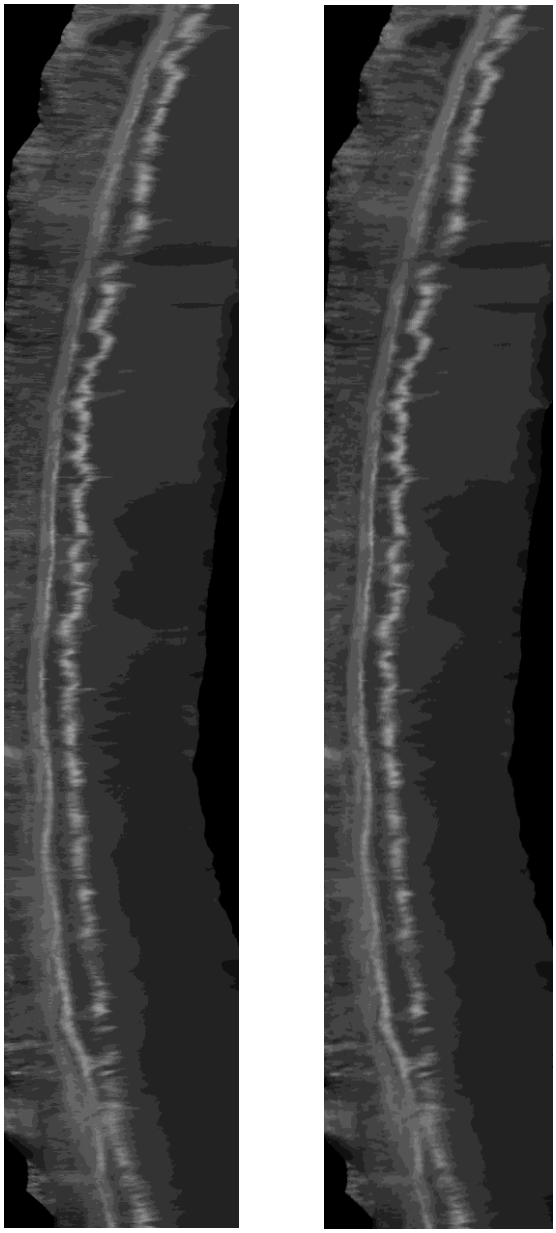

Figure 11: A time-averaged mosaic section rotated to a baseline coordinate system (left) with 20 *m* alongshore averaging (right).

and FRF bathymetric survey data were utilized to test the data assimilation methods. Pixel intensity profiles can be extracted from a mosaic to overlay either gridded or FRF bathymetry profiles by selecting the appropriately indexed image matrix (Figure 12). For final

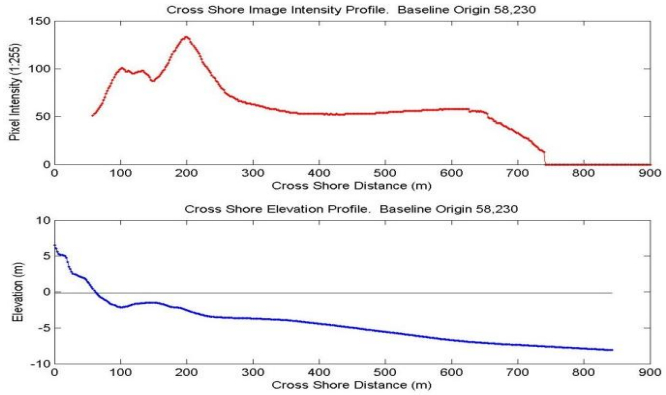

Figure 12: A plot showing a pixel intensity profile extracted from a time-averaged mosaic (above) and corresponding FRF crosshore bathymetry profile (below).

analysis, a single mosaic was compiled that covered the area of the FRF survey and was then rotated to the FRF local baseline coordinate system (Figure 13). The mosaic is then manually checked against several GPS ground points along the FRF pier for alignment issues and, if necessary, shifted accordingly. The individual transects that comprise an FRF data set follow a general, but not exact, shore normal path. The average alongshore coordinate of a surveyed profile was used to extract pixel intensities in a straight transect for analysis without introducing any significant error (Figure 13).

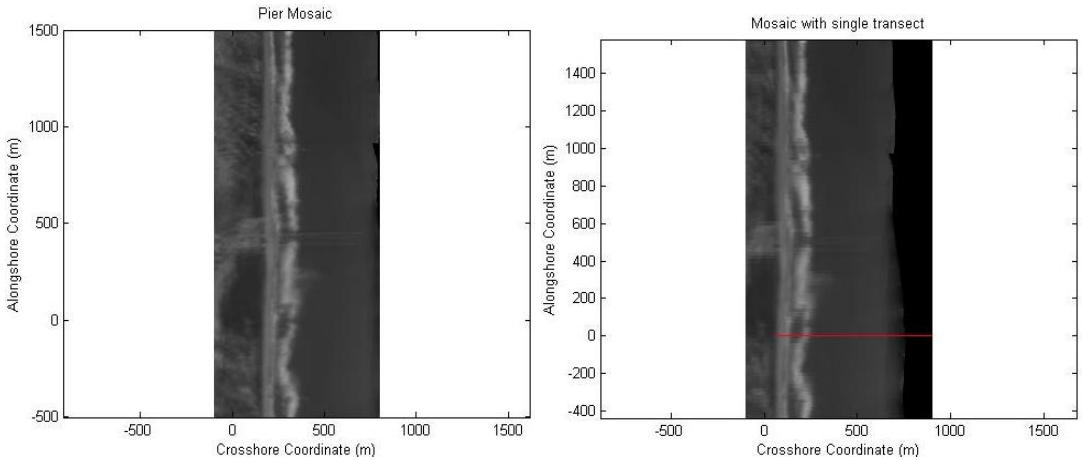

Figure 13: A time-averaged mosaic of the FRF surveyed coastline rotated to a local coordinate system as defined by the FRF (left) and an example of a time-averaged mosaic with transect line corresponding to the location of an FRF surveyed profile (right).

The wave model used in this work (described previously) requires information about tide level, offshore wave height, wave angle, and spectral peak wave frequency. This information was obtained from an established *in situ* pressure sensor array located in 8 *m* water depth at the FRF field site. The 8 *m* array data produces directional wave information at 3-hour intervals, which were used to extract wave information at times where the AVS imagery was collected. The wave model also requires three user defined variables γ, B, and σ. The parameter γ is a saturation constant that is largely constrained by observation to values between 0.32 and 0.42 and is taken to be 0.38 following Lippmann, *et al*. (1996). B is a variable describing the fraction of the wave face covered by the wave roller and is given the constant value of 1. The final variable σ is the angle of the wave/roller interface and is an important adjustable parameter in the overall assimilation scheme. Changing the angle of the wave roller interface changes the distribution of dissipation and was initially chosen at a value of 10 degrees.

The assimilation routine begins by taking an assigned FRF profile data set (with data removed from the surf zone) and initially estimating the surf zone bathymetry, *h*, as a function of crosshore coordinate, *x*, using a hyperbolic tangent equation defined by Lippmann *et al.* (1999).

$$h = x\tan\beta_2 + \frac{a_1}{\tan\beta_2}(\tan\beta_1 + \tan\beta_2)\tanh\left(\frac{x\tan\beta_1}{a_1}\right) \quad (8)$$

This function uses values for foreshore slope, $\beta_1 = 0.10$ and offshore slope, $\beta_2 = 0.008$ that are typical of North Carolina beaches near the FRF. A value for the coefficient a_1 is then calculated using the elevation of surveyed points just before and after the surf zone. This hyperbolic tangent function creates a smooth curve estimate of the surf zone bathymetry (Figure 14), which is used instead of a linear interpolation because the wave model tends to work better when it is forced to accrete rather than erode. Image intensity profiles are then selected from a time-averaged mosaic

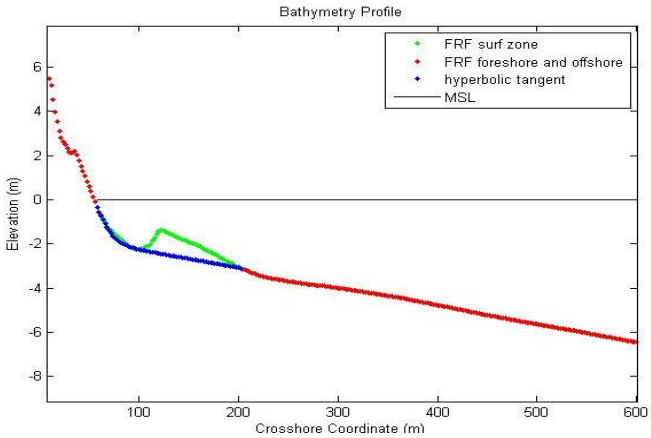

Figure 14: A plot showing an actual FRF surveyed crosshore bathymetric profile and initially estimated bathymetry used to replace surf zone data.

which overlays the FRF bathymetry profiles. This mosaic will have been created from AVS imagery collected on the date closest to that of the FRF bathymetry survey. A single bathymetric profile and all necessary parameters are input into the wave model which calculates the wave

dissipation. The intensity profile is scaled and compared to the dissipation profile calculated by the wave model.

The initially estimated bathymetry is then updated as a function of the difference between image intensity and calculated dissipation, as well as distance from the midpoint of the surf zone. In addition, the bathymetry update exponentially decreases at distances within a quarter of the profile length from the shoreline. This process is repeated for each profile in the data set until the difference between image intensity and modeled dissipation are acceptable based on three criteria: (1) a maximum RMS error value less than 10 *cm*, (2) both a mean RMS error less than 10 *cm* and a RMS error less than 2 *cm* at the location of the peak intensity, or (3) 32 iterations (Figure 15-16). The RMS error requirements between numerical dissipation and scaled intensities used to stop the assimilation routine were determined empirically to produce the best results. A smoothing algorithm checks assimilated profiles for sharp spikes in bathymetry unlikely to exist in reality and then saves each final profile as a x,y,z column formatted text file.

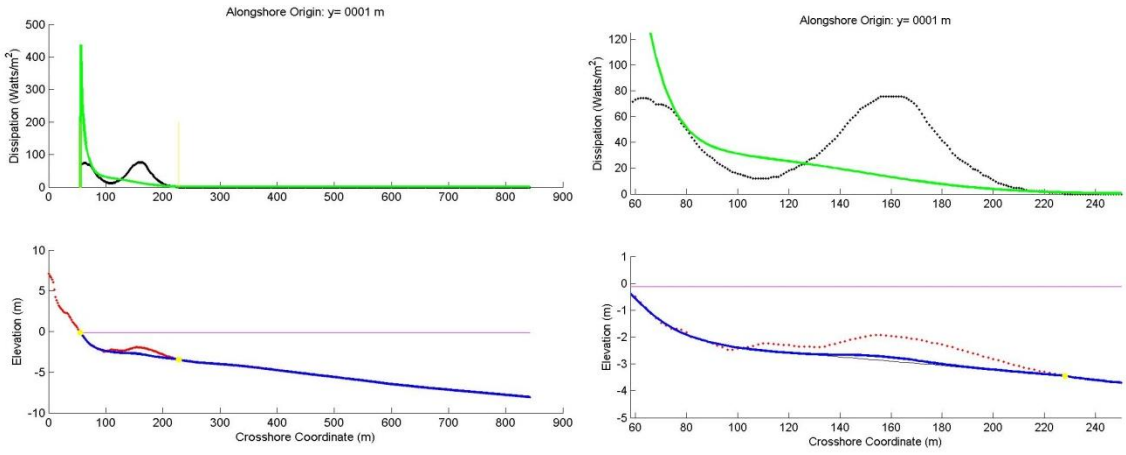

Figure 15: A plot of scaled image intensity (black, *watts/m*^{2}) and initial wave model dissipation (green, *watts/m*^{2}) above left with actual (red, *m*) and initially estimated (blue, *m*) crosshore bathymetric profiles shown (below left). The same figure is showed zoomed in to the surf zone region of the profile (right).

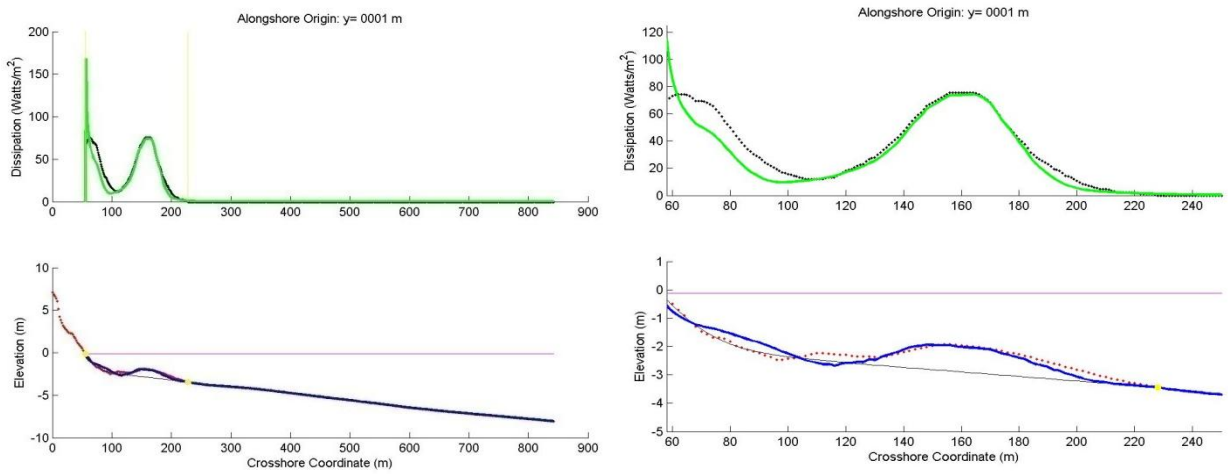

Figure 16: A plot of scaled image intensity (black, *watts/m*^{2}) and final wave model dissipation (green, *watts/m*^{2}) above left with actual (red, *m*) and final estimated (blue, *m*) crosshore bathymetric profiles shown (below left). The same figure is showed zoomed in to the surf zone region of the profile (right).

III. Results

FRF bathymetry surveys from 17 April 2002, 08 January 2003, and 19 April 1999 were used in conjunction with multiple north/south pass AVS data sets collected on 13 April 2002, 16 January 2003, and 16 April 1999, respectively. While mosaics were created for several other dates, the listed data sets were used in the analysis because of the availability of FRF bathymetry sets surveyed within a relatively short time period of the AVS flight. The RMS error of assimilated bathymetry profiles were calculated individually and as an average over the entire data set by comparison to the actual surveyed FRF profile data. The average RMS error in bathymetry over the range of the entire data set was typically around 35 *cm*, with optimal results being approximately 25 *cm*. RMS errors for individual estimated bathymetry profiles varied widely from around 10 *cm* to more than 100 *cm* in some instances. The assimilation routine regularly estimated the general shape of simple barred bathymetric profiles. Where the actual bathymetry possessed multiple bars, a steep sloped bar, or any other odd features, the assimilation routine typically missed the general shape of the profile.

For further analysis, the individual profiles of a data set were triangularly interpolated onto an evenly spaced grid spanning the FRF survey region. This gridded data was plotted with contours in order to examine alongshore and larger scale bathymetric features that are not considered when looking at individual crosshore profiles (Figure 17). Contoured plots of bathymetry initially estimated using the hyperbolic tangent function and actual FRF surveyed bathymetry (Figure 17) were also created in the same manner for comparison with the assimilated data. Compared to the actual bathymetry contour plots, the assimilated data appears to roughly predict the correct location and to a lesser degree the shapes of larger scale bathymetric features (Figure 17). Analysis of difference plots created by subtracting FRF

surveyed bathymetry from initially estimated bathymetry (Figure 18) and assimilated bathymetry estimates (Figure 18) shows that the assimilation process has the effect of reducing the overall RMS error of initially estimated bathymetry by a factor of approximately 2.

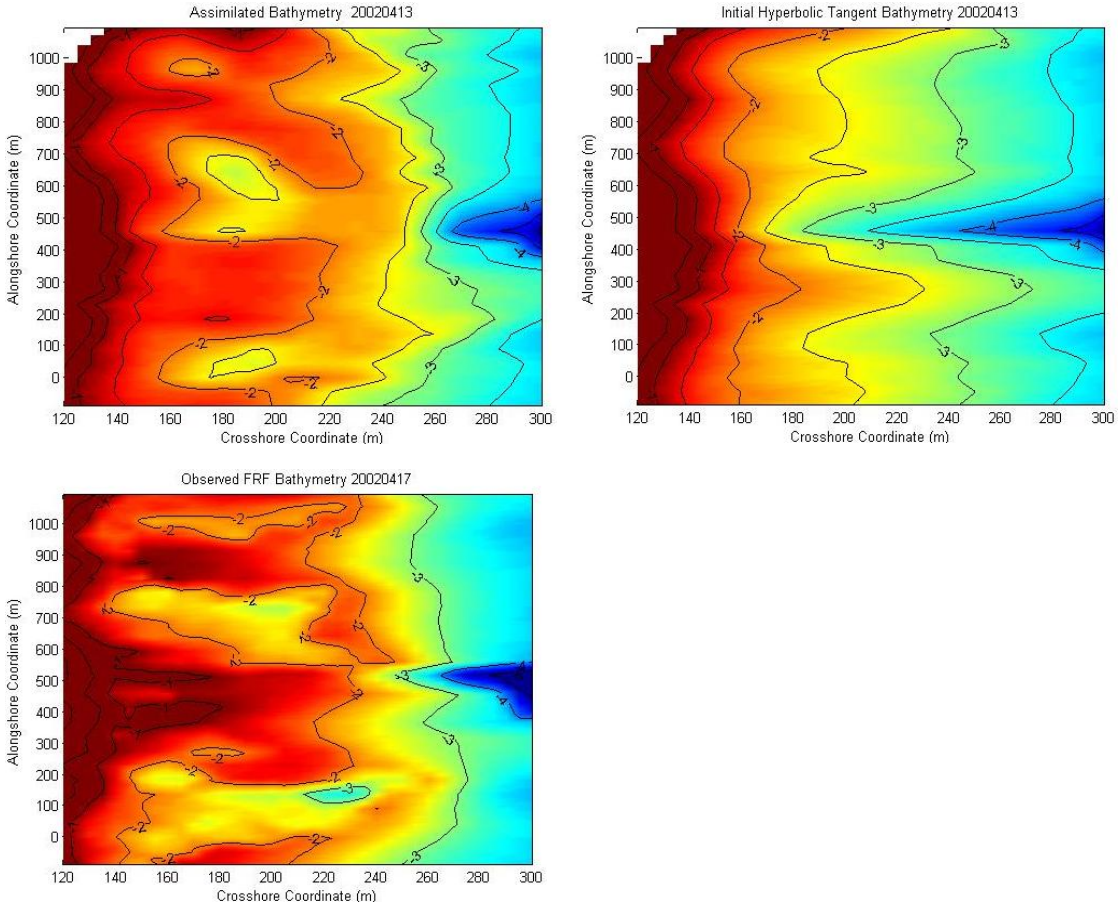

Figure 17: A contour plot of the FRF surf zone created from a data set of assimilated bathymetric profiles from 2002/04/13 (top left), a contour plot of the FRF surf zone created from a data set of intially estimated bathymetric profiles from 2002/04/13 (top right), and a contour plot of the FRF surf zone created from a data set of FRF surveyed bathymetric profiles from 2002/04/17 (bottom left). Crosshore coordinate is given for the x-axis and alongshore coordinate for the y-axis in all figures.

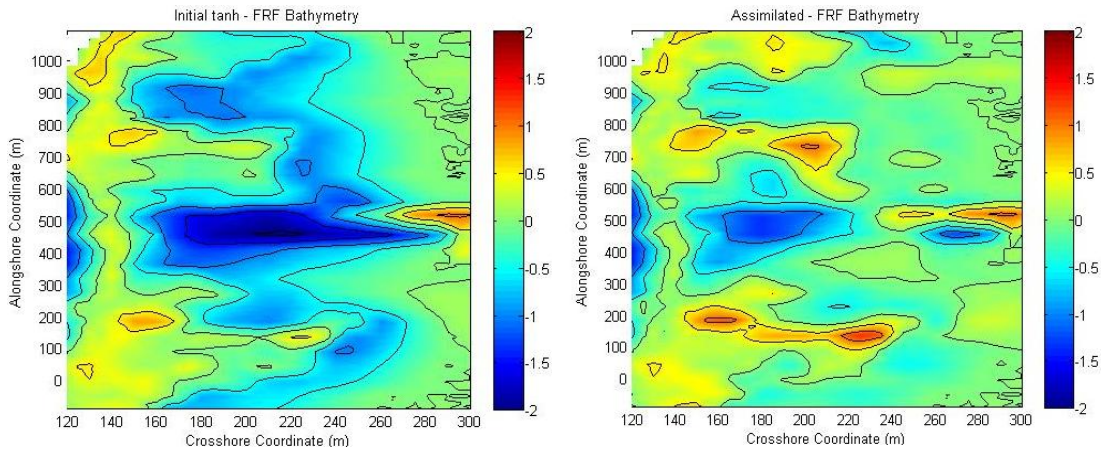

Figure 18: A contoured difference plot of the FRF surf zone between initially estimated bathymetry from 2002/04/13 and FRF surveyed bathymetry from 2002/04/17 (left) and a contoured difference plot of the FRF surf zone between assimilated bathymetry from 2002/04/13and FRF surveyed bathymetry from 2002/04/17(right). Crosshore coordinate is given for the x-axis and alongshore coordinate for the y-axis in both figures. A contour color map is given for each figure as well.

To check for biases in our methods, both RMS error for assimilated and initially estimated bathymetry were plotted as a function of their alongshore (Figure 19) and crosshore coordinates (Figure 19). In plotting RMS errors as a function of alongshore coordinate, data constantly revealed that there was an increase at approximately 500 *m*. This is very close to the coordinate of the FRF pier and it is very likely that a lack of surveyed data in this region biased our RMS error calculations. In the crosshore direction, RMS errors near the edges of region examined remained similar for both assimilated and initially estimated data, which was to be expected, because the assimilation routine updates bathymetry as a function of distance from known points fixed on the edge of each profile. In many cases, data also showed a smaller increase in error near the shoreline that is most likely caused because the wave model forces dissipation to zero at the shoreline. Plotting RMS error as a function of crosshore coordinate also illustrates that there is a significant reduction in error in the middle of the surf zone where the model accretes barred features not present in the initially estimated bathymetry.

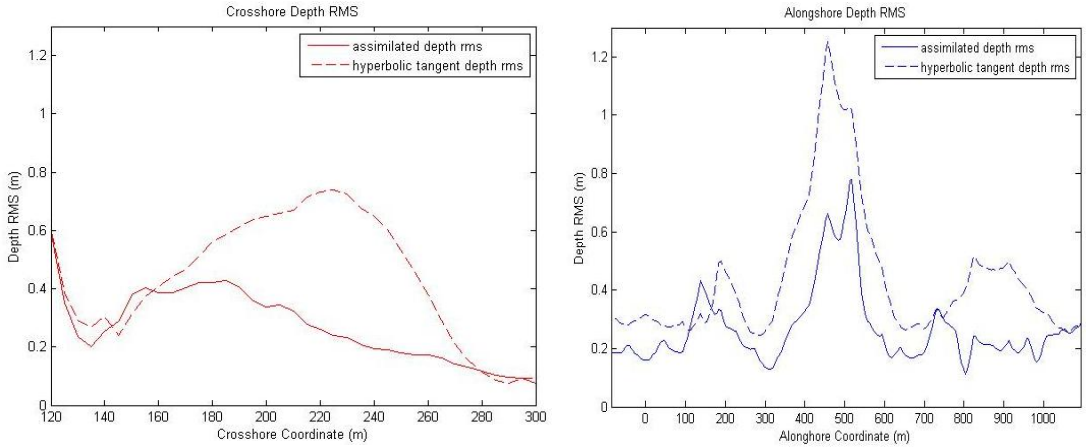

Figure 19: Bathymetry RMS error plotted as a function of crosshore coordinate for both initial and assimilated bathymetric estimates (left), and bathymetry RMS error plotted as a function of alongshore coordinate for both initial and assimilated bathymetric estimates (right). Data for both plots was collected between 2002/04/13 and 2002/04/17.

The effects of changing the initial parameters γ, B, and σ were tested to find values that optimized the capability of the assimilation routine. Average RMS error values for bathymetry were calculated over a range of σ values from 0.5 - 20 degrees (Figure 20). Results showed that except for extreme values, σ had less impact on the assimilation routine than was expected. A value of 4 was eventually decided on to produce the lowest RMS error values and was used for all final analysis. Testing of B and γ revealed that the initial values used for these parameters were acceptable.

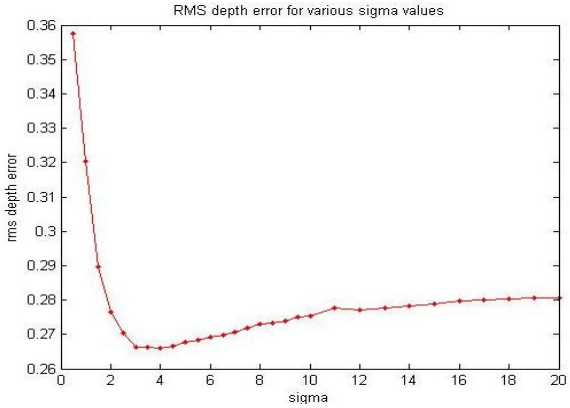

Figure 20: Average bathymetric RMS error plotted as a function of sigma showing optimal results around four degrees.

IV. Conclusions

Although the data used for this work does not come from intended LIDAR sources, the results suggest that such an assimilation technique could be used for estimating surf zone bathymetry for incomplete LIDAR surveys. Time-averaged mosaics created from airborne video data showed results that are comparable with similar assimilation techniques that use land-based video systems. There remain many questions about the use of an assimilation process with airborne video data that will require future testing in order to be answered. These questions leave room for both the improvement and dismissal of the practical capabilities of this assimilation method to improve airborne LIDAR bathymetric estimation.

The assimilation process is highly dependent on the quality of video data and the alignment of mosaics created from them. The ideal data collection methods for LIDAR topographical data and video data seem to contradict each other. Digital video data used to create time-averaged mosaics must have a longer dwell time than currently provided. If there is no way to reconcile this issue, the technique of data assimilation using airborne LIDAR AVS may simply become an impractical option for improving LIDAR data collection. Imagery collected by airborne LIDAR systems does, however, have much more accurate GPS/INS synchronization than the video data used in this work. It is reasonable to hypothesize that the use of airborne LIDAR video data would improve upon image geo-referencing and mosaic alignment, potentially reducing error in final bathymetry estimates. It should also be noted that the inherent source of error incurred in this work from using surveyed data and video data collected on different days would be eliminated if video data collected simultaneous with LIDAR data were used.

The use of actual airborne LIDAR bathymetric data rather than FRF surveyed data will add a certain amount of error into the process as well. The RMS error of FRF surveyed data is around 10 *cm*, while airborne LIDAR has an RMS error around 15 *cm*, introducing a net increase in RMS error of approximately 5 *cm*. Obtaining initial offshore wave conditions from published data limits the area of usefulness of assimilation techniques to locations where such data are collected. The potential to gather this type of information from LIDAR sea surface return data could make the process autonomous, giving it the capability to operate anywhere. This would require special attention because the wave model seems to be sensitive to these initial conditions.

The assimilation routine appears to work generally well, especially in cases with simple bathymetric profiles and where accretion of the initial bathymetry is the primary assimilation mode. Adding terms to account for setup (the super-elevation of the mean water surface) may improve the wave model's capability near the shoreline where forcing the dissipation to zero in the current model is not realistic. Finally, the model parameters have all been fixed to produce optimal results for a very specific beach profile and need to be tested in other geographical locations.

The need to better understand nearshore coastal evolution, combined with continual advances in technology, will eventually lead to better methods of bathymetric survey in the surf zone. While the practicality of such a method is left open, it has shown potential in estimating larger scale bathymetric features with reasonable accuracy. The assimilation technique will ultimately need to be tested with actual LIDAR video and bathymetric data It will require continued work to conclude whether or not the process of assimilation of airborne LIDAR data for bathymetric estimation is a worthwhile avenue to pursue.

V. References

Aarninkhof, S. G. J., B. G. Ruessink, 2004, Video Observations and Model Predictions of Depth-Induced Wave Dissipation, IEEE *Trans. Geosci. Remote Sens*., 42, 2612-2622.

Aarninkhof, S. G. J., B. G. Ruessink, and J. A. Roelvink, 2005, Nearshore Subtidal Bathymetry From Time-Exposure Video Images, *J. Geophys*. Res., 110, C09011, doi:10.1029/2004JC002791.

Dalrymple, R.A., 2003. Trends in Coastal Engineering in the US, Proceedings Toward New Progress in Coastal Engineering in Japan.

Deigaard, R., 1993, A Note On the Three-Dimensional Shear Stress Distribution in Dissipative Water Waves, *Coastal Engineering*, 20, 157-171.

Houston J.R., 1996. International Tourism and U.S. Beaches, Coastal Engineering Research Center Vicksburg, MS. Tech report, AD-A314 680, 1-7.

Irish J.L McClung J.K., and Lillycrop W.J., 2000. Airborne LIDAR Bathymetry: The SHOALS System.

Kraus N. C. and McDougal W. G., 1996, The Effects of Seawalls on the Beach: Part1, an Updated Literature Review, *Journal of Coastal Research*, vol.12, 3, 691-701.

LeMahaute, B., 1962, On Non-Saturated Breakers and the Wave Run-Up, in *Proceedings of the 8th International Conference on Coastal Engineering*, Amer. Soc. Civ. Eng., New York, 77-92.

Lippmann, T. C., R. A. Holman , 1989, Quantification of Sand Bar Morphology: A Video Technique Based on Wave Dissipation, *JGR*, 94(C1), 995-1011.

Lippmann, T. C., A. H. Brookins, and E. B. Thornton, 1996, Wave Energy Transformation On Natural Profiles, *Coastal Engineering*, 27,1-20.

Lippmann, T. C., T. H. C. Herbers, and E. B. Thornton,1999, Gravity and Shear Wave Contributions to Nearshore Infragravity Motions, *J. Geophys*., 231-239.

Morris, Thompson M., *Manual of Photogrammetry Third Edition Vol.*I. Falls Church, VA: American society of Photogrammetry, 1966.

Roelvink, D., S. Aarninkhof, A. J. M. Reniers, N. Plant, R. A. Holman, T.C. Lippmann, E. B. Thornton, G. Symonds, and S. Frazier, 2006. Beach Wizard: A Prototype Coastal Ocean Observing System, *Proc. 12th Canadian Coastal Conference*

Svendsen, I. A., 1984, Wave Heights and Set-Up in a Surf Zone, *Coastal Engineering*, 8, 303-329.

Thornton, E. B., and R. T. Guza, 1983. Transformation of Wave Height Distribution, *J. Geophys. Res, 88, 5925-5938*.

Thornton, E. B., and R. T. Guza, 1986, Surf Zone Longshore and Random Waves: Field Data and Models, *J. Phys. Oceanogra*., 16(7), 1165-1178.

Van Dongeren, A., Plant, N., Cohen, A., Roelvink, D., Haller, M., Catalan, P., in review, Beach Wizard: Nearshore Bathymetry Estimation Through Assimilation of Model Computations and Remote Observations, *Coastal Engineering*.

Whitford, D. J., 1988, Wind and Wave Forcing of Longshore Currents Across a Barred Beach, *Ph.D. Thesis*, Naval Postgraduate School, Monterey, CA, pp. 205.

Worley C. R., T. C. Lippmann, J. W. Haines, A. H. Sallenger, 1997, An Aerial Video System For Rapidly Measuring the Spatial Variability of Very Large Scale (10^1-10^3 KM) Sand Bar Morphology, *Coastal Dynamics*, 1-8.

Worley C. R., T. C. Lippmann, J. W. Haines, A. H. Sallenger, 1998, The Spatial Variability of Large Scale Sand Bars, *Proceedings of the 29th International Conference on Coastal Engineering*, Amer. Soc. Civ. Eng., New York, 1-12.